Journal of Materials Chemistry A

A biocompatible open system Na-doped IrOx(OH)y energy storage device with enhanced charge storage properties and long lifetime

Journal:	*Journal of Materials Chemistry A*
Manuscript ID	TA-ART-05-2022-003603.R1
Article Type:	Paper
Date Submitted by the Author:	08-Jun-2022
Complete List of Authors:	Hsieh, Yi-Chieh; National Yang Ming Chiao Tung University, Materials Science and Engineering Lai, Chun-Han; University of California Los Angeles, Department of Materials Science and Engineering Tso, Kuang-Chih; National Yang Ming Chiao Tung University, Graduate Program for Science and Technology of Accelerator Light Source Chou, Shih-Cheng; National Chiao Tung University Whang, Grace; University of California Los Angeles Choi, Christopher; University of California, Los Angeles, Materials Science and Engineering Cheang, Wai-Hong; National Yang Ming Chiao Tung University Chu, Chao-Yi; Chiao-Tung University, Department of Materials Sciences and Engineering Lee, Jyh-Fu; National Synchrotron Radiation Research Center, Experimental Facility Division Chen, Po-Chun; National Taipei University of Technology Chen, San-Yuan; National Chiao Tung Universit, Department of Materials Sciences and Engineering Dunn, Bruce; University of California, Dept of Materials Sci and Eng Wu, Pu-Wei; National Chiao Tung University,

ARTICLE

A biocompatible open system Na-doped $IrO_x(OH)_y$ energy storage device with enhanced charge storage properties and long lifetime

Received 00th January 20xx,
Accepted 00th January 20xx

DOI: 10.1039/x0xx00000x

Yi-Chieh Hsieh,[a] Chun-Han (Matt) Lai,[b] Kuang-Chih Tso,[c,d] Shih-Cheng Chou,[a]

Grace J. Whang,[b] Christopher S. Choi,[b] Wai-Hong Cheang,[a] Chao-Yi Chu,[a]

Jyh-Fu Lee,[e] Po-Chun Chen,[f] San-Yuan Chen,[a] Bruce S. Dunn,*[b] Pu-Wei Wu,*[a]

Reliability of an energy storage device has been the top requirement for implantable biomedical devices. Conventional implantable batteries have generated serious concerns over their long-term biocompatibility because of potential package corrosion and electrolyte leakage. Here, we demonstrate an open system device using body fluid as the electrolyte that addresses the biocompatibility and reliability issues simultaneously. First, we fabricate Na-$IrO_x(OH)_y$ biocompatible electrodes by a simple and scalable wet chemical approach. A series of operando measurements were used to establish chemical reactions and structural changes associated with the Na-$IrO_x(OH)_y$. An impressive charge storage capacity (1,187 C g^{-1}/330 mAh g^{-1}) is achieved by multiple redox reactions, including the proton and Na ion insertion/extraction that reaches >10,000 cycles in both phosphate buffered saline and L929 cell culture. To validate the biocompatibility of Na-$IrO_x(OH)_y$, symmetric full cell devices are fabricated on flexible Au-coated polypropylene micromembranes and operate in a L929 cell solution. The open system device reveals a battery-like capacity of 295 mC cm^{-2} with an energy density of 3.4 mWh cm^{-3}. In addition, the L929 cells stay alive over 72 h. The successful demonstration of Na-$IrO_x(OH)_y$ full cells has underscored the potential of developing open system energy storage devices for next-generation implantable power sources.

Introduction

The Internet of Things (IoT), which relies on information exchange among devices, has not only promoted the growth of consumer electronics but also has enabled significant improvements in both the healthcare sector and point-of-care testing.[1,2] In offering expanded patient services, such as self-monitoring and therapeutics, the market forecast for healthcare IoT systems is expected to grow to 534.5 billion USD by 2025.[3] Although the combination of miniaturized microelectronics and biocompatible materials has fostered the successful integration of microbial electrochemical systems into implantable biomedical devices,[4] biocompatible power supplies for these implantable devices have lagged behind. Ever since the first miniature battery for implantable biomedical devices was commercialized in the 20th century,[5-8] biocompatibility concerns over additional surgeries and battery leakage have challenged the development of implantable power sources. The surgical concern has been addressed by the adoption of external wireless charging and secondary batteries, but even with advanced leakage-proof packaging, these in-body power sources still have potential biocompatibility problems due to parasitic corrosion from their packaging materials.[6,9,10]

Recently, open system power supplies have shown great potential to meet the biocompatibility requirements while eliminating the exposure of harmful electrolyte.[9,11-13] The ideal design for such a system is to immerse biocompatible energy storage materials in body fluids serving as the electrolyte without any packaging. For example, protein-based batteries and supercapacitors use biofriendly carbonaceous materials including carbon nanotubes, graphene sheets, and carbon fibers for their well-studied cytotoxicity.[11,13-18] Unfortunately, the low energy density of these carbon-based materials has become the major limitation in the miniaturization of implantable biomedical devices. While these carbon-based power supplies exhibit improved power density and cycling stability, their energy density and volumetric capacitance without packaging remain significantly lower in comparison with conventional closed system counterparts. Another possible open system power supply which might deliver the necessary energy is biogalvanic cells or biofuel cells. These devices are normally used for short term treatments such as

[a] Department of Materials Science and Engineering, National Yang Ming Chiao Tung University, Hsinchu 30010, Taiwan.
[b] Department of Materials Science and Engineering, University of California, Los Angeles, California 90095, United States.
[c] Graduate Program for Science and Technology of Accelerator Light Source, National Yang Ming Chiao Tung University, Hsinchu 30010, Taiwan.
[d] Division of Materials Science, Graduate School of Science and Technology, Nara Institute of Science Technology, Nara 630-0192, Japan.
[e] National Synchrotron Radiation Research Center, Hsinchu 30076, Taiwan.
[f] Department of Materials and Mineral Resources Engineering, National Taipei University of Technology, Taipei 106203, Taiwan.

Electronic Supplementary Information (ESI) available: [details of any supplementary information available should be included here]. See DOI: 10.1039/x0xx00000x

drug delivery due to their limited cycle life.[19,20] Thus, because of limitations in energy density and cycle life, a reliable open system power supply operating in the human body has yet to be developed.

Pseudocapacitors are a class of electrochemical energy storage materials that have demonstrated both high energy and power density through their intrinsically fast faradaic redox reactions.[21,22] In particular, the hydrous derivative of iridium oxide, $IrO_x(OH)_y$, has been reported to be a pseudocapacitive material and a mixed electronic-protonic conductor, where protons migrate through the hydrous boundaries during the charge storage process.[23,24] This material benefits from the fact that IrO_2 is known for its biocompatibility and chemical inertness under *in-vivo* conditions.[25,26] With appropriate processing, the $IrO_x(OH)_y$ could be prepared as nanoscale films, which enables rapid charge storage kinetics similar to that of conventional electrical double-layer capacitors (EDLC) but with an energy density comparable to a typical battery material.[27,28] For example, IrO_2 films prepared by plasma enhanced chemical vapor deposition demonstrated a capacity of 293 C g^{-1} (81 mAh g^{-1} in 7 min charge/discharge),[28-31] while the activated $IrO_x(OH)_y$ films revealed a capacity of 715 C g^{-1} (199 mAh g^{-1} in 56 s charge/discharge).[32-34] In addition, $IrO_x(OH)_y$ nanofilms from wet chemical bath deposition delivered a capacity of 798 C g^{-1} (221.7 mAh g^{-1} in 2 min charge/discharge).[35] Furthermore, recent studies indicate that by doping with alkali ions, the Na or K-doped IrO_2 have exhibited reduced redox overpotentials, and exhibit greatly improved oxygen evolution reaction kinetics.[36,37] The concept of utilizing doping ions for rapid pseudocapacitive storage has also been reported by Tarascon et al. as the layered Li_3IrO_4 structure extends insertion reactions to 3.5 electrons per Ir atom in a nonaqueous electrolyte.[23] However, after acid leaching, their $H_{3+x}IrO_4$ is only capable of 1.7 electrons per Ir atom in an aqueous solution. Hence, in addition to having a higher specific capacitance for $IrO_x(OH)_y$, the insertion/extraction of alkali ions (Na^+ or K^+) from the electrolyte also play an important role for biocompatibility.[13,14,38] With higher energy density, fast kinetics, and improved biocompatibility, the $IrO_x(OH)_y$ represents a promising material for an open system power supply.

In this work, we develop a biocompatible open power supply using sodium-doped $IrO_x(OH)_y$ (Na-$IrO_x(OH)_y$) as the electrode material. Different from conventional IrO_2 derivatives, our Na-$IrO_x(OH)_y$, prepared via a wet chemical bath, possesses an amorphous structure and a relatively large capacity of 1,187 C g^{-1} (330 mAh g^{-1}, equivalent to 2.7 electrons per Ir atom). Two different types of Na-$IrO_x(OH)_y$ electrodes, thin films and flexible porous electrodes, were investigated as components in an open system energy storage device. The thin film electrodes were used to understand the structural changes and charge storage mechanism of Na-$IrO_x(OH)_y$ associated with the Ir valence states that are influenced by the insertion/extraction of protons and Na ions, whereas the thick flexible electrodes were fabricated into a symmetric full cell cycled *in-vivo* to mimic energy storage applications in a real human body. The Na-$IrO_x(OH)_y$ device exceeds the energy density and life span of alternative open system devices,[11,13,14-16,39-41] offering the potential of serving as a critical power source for implantable biomedical devices.

Experimental

Wet chemical deposition of Na-$IrO_x(OH)_y$ electrodes

Deposition of Na-$IrO_x(OH)_y$ was carried out through a wet chemical bath. In brief, a 1×2 cm^2 Au-coated substrate (Si wafer or polypropylene micromembrane (PPMM)) was immersed in a 9.6 mL aqueous solution, which contained 17.04 mg (3.4 mM) potassium hexachloroiridate (III) (K_3IrCl_6, Alfa Aesar), 9.21 mg (3.4 mM) sodium potassium tartrate ($KNaC_4H_4O_6{\cdot}4H_2O$, Sigma Aldrich), 38.4 mg (0.1 M) sodium hydroxide (NaOH, Alfa Aesar), and 2.4 g (0.4 M) sodium hypochlorite (NaClO, Sigma Aldrich). Those chemicals were mixed sequentially to initiate the following oxidation and reduction processes. Specifically, the Ir precursor, K_3IrCl_6, was first dissolved in deionized water, followed by adding the complexing agent $KNaC_4H_4O_6$. After the solution was thoroughly mixed, the NaOH was added to adjust the pH value to 13, and the NaClO as the oxidizer was added to complete the precursor solution. Once the substrate was immersed in the solution, the redox reactions (Ir (III) to Ir (V), then to Ir (IV)) took place immediately, forming a Na-$IrO_x(OH)_y$ thin film on the Au surface. The entire deposition process was conducted at 25°C for 1 h. Upon finished, the sample was removed from the solution, washed thoroughly with deionized water, and dried with air blow before further test. The same deposition process was also carried out on a Au-coated AT-cut quartz crystal substrate to determine the weight of Na-$IrO_x(OH)_y$ using a quartz crystal microbalance. To fabricate thick and flexible electrodes, Na-$IrO_x(OH)_y$ was deposited on Au-coated PPMM (Au-PPMM) using the same synthetic method. The substrate was immersed in a freshly made precursor solution for 1 h to complete one layer of deposition, followed by identical cleaning and drying steps. The entire deposition process was repeated for 5 times on each Na-$IrO_x(OH)_y$-Au-PPMM flexible electrode to achieve the desirable loading (~1 mg/electrode) before assembling the full cell.

Sputter deposition of IrO_x electrodes

The pure IrO_x films were fabricated on Ti-coated Si wafer by sputtering from an Ir target. The gas ratio of Ar to O_2 was 1:100 with chamber pressure at 7.6×10^{-2} Pa and power of 100 W. The sputtering process lasted for 1 h, resulting in a 400 nm thickness.

Materials characterization

Energy-dispersive X-ray spectroscopy (EDX) equipped scanning electron microscopes (SEM; Nova NanoSEM 230, FEI and JSM-6700F, JEOL) were used to characterize the surface morphology and elemental distribution of Na-$IrO_x(OH)_y$ thin film. Fourier-transform infrared spectroscopy (FT-IR; FT/IR-6100 spectrometer, Jasco) was performed in 3,200 to 500 cm^{-1} to identify the presence of iridium oxide and oxohydroxide. Thermogravimetric analysis (TGA; SDT Q-600, TA Instruments) was employed on Na-$IrO_x(OH)_y$ powders to determine the

amount of oxohydroxide and residual moisture content in the as-prepared samples. Synchrotron X-ray diffraction (SXRD) analysis on Na-$IrO_x(OH)_y$ was conducted at the National Synchrotron Radiation Research Center (NSRRC, Hsinchu, Taiwan) using the BL01C2 beamline (0.826569 Å). The *in-situ* XRD patterns for as-synthesized and annealed samples were recorded by an imaging plate detector (Mar345) with a counting period of 600 s under a heating rate of 5°C min^{-1}. The one-dimensional powder diffraction profile was converted using a GSAS II program and was calibrated according to Bragg positions of LaB6 (SRM-660C) standard.

Electrochemical analysis

Electrochemical characterization of Na-$IrO_x(OH)_y$ and sputtered IrO_x were carried out using a three-electrode setup. For half-cell test, the thin film electrodes were studied in a PBS (1X, Corning) with a Pt mesh counter electrode (1.5×0.4 cm2) and a saturated Ag/AgCl reference electrode (3M NaCl). Symmetric full cells which comprised two identical thick flexible Na-$IrO_x(OH)_y$ electrodes were also prepared with the PBS for mechanistic study and cycle life test. Cyclic voltammetry (CV) and galvanostatic charge-discharge (GCD) were conducted using VMP potentiostat/galvanostat (Bio-Logic) and Versastat 4 potentiostat between -0.6 and 0.8 V (vs. Ag/AgCl) for a half cell and -0.8 to 0.8 V for a full cell. Specific capacity (C g^{-1}) for Na-$IrO_x(OH)_y$ was determined from their CV profiles using the following equation (1) and from GCD profiles with equation (2):

$$C = \int_{V_1}^{V_2} \frac{I dV}{mv} \quad (1)$$

$$C = \frac{I\Delta t}{3.6 \times m} \quad (2)$$

where the V_1 and V_2 are the initial and final potentials for selected redox reactions, the I (A) is the current within the potential range, the v is the sweep rate (V s^{-1}), the m is the sample mass, and the Δt is for time (s).

Energy and power densities were obtained from GCD profiles, and were calculated with following equations:

$$SE = \frac{1}{2} CV^2 \quad (3)$$

$$SP = \frac{E}{\Delta t} \times 3600 \quad (4)$$

where the *SE* is specific energy density (Wh cm^{-2}), the *C* is the specific capacitance (F cm^{-2}), the *V* is the potential window (V), the *SP* is the specific power density (W cm^{-2}), and th Δt is the discharge time (s). In this work, only the positive potential (0 to 0.8 V) was used to calculate the energy and power densities.

eQCM analysis

For eQCM study (eQCM 10M, Gamry), Au coated AT-cut quartz crystals were adopted as the substrate for depositing Na-$IrO_x(OH)_y$ via the same deposition method as mentioned before. Each pristine quartz crystal was calibrated with a calibration constant (C_f) of 56.6 MHz cm^2 g^{-1} in the Sauerbrey equation. The Na-$IrO_x(OH)_y$-coated quartz crystal electrode was served as the working electrode and tested in a commercial temperature controlled cell (SKU 990-00400, Gamry) with a three-electrode setup (Pt counter and Ag/AgCl (3M NaCl) reference electrodes) at 24±2°C. The electrode area exposed to the electrolyte was 1.1 cm^2, along with a smaller piezoelectrically active area of 0.24 cm^2. Each measurement was performed using CV at 10 mV s^{-1} between -0.4 and 0.7 V vs. Ag/AgCl in 0.5 M Na_2HPO_4 aqueous solution. Five CV cycles within the full potential range were performed to form a stable surface condition to obtain the exact mass change for each redox couple. The mass change (Δm) was determined by converting the frequency change (Δf) using the Sauerbrey equation ($\Delta m = -C_f \cdot \Delta f$). The variation in current was monitored simultaneously during the process, and was further integrated into the charge at each potential. The linear charge-mass dependency was determined from the slope, via the equation (5) listed below, indicating the molecular mass (*MM*) of transferred species:

$$MM = nF\frac{\Delta m}{\Delta Q} \quad (5)$$

where the *n* is the number of transferred electrons, the *F* is the Faraday constant, and the ΔQ is the variation in coulomb charge.

***Operando* and *ex-situ* X-ray spectroscopy**

The *operando* XAS measurements were conducted at the BL17C1 beamline of NSRRC with ring energy of 1.5 GeV and emission current of 300-360 mA in a fluorescence mode with a 3-mm-thick Zn filter and a detector targeting the LIII-edge of Ir (11,215 eV). A 100-nm-thick Na-$IrO_x(OH)_y$ thin film on an indium tin oxide (ITO) substrate was prepared using the same plating solution with multiple deposition steps. A polytetrafluoroethylen (PTFE) cell was designed to detect the absorption signal with minimal energy absorption of electrolyte under various imposed potentials. During measurements, the Na-$IrO_x(OH)_y$ thin film was cycled in a PBS using CV (50 mV s^{-1}) between -0.6 and 0.8 V, followed by holding the potential at selected values until the measurement was finished. The XAS analysis started after 1,000 s of potential holding and repeated three times before switching to next potential. The duration for entire XAS analysis lasted for 2 h. The valence states of Ir atoms were evaluated using commercial $IrO_2 \cdot H_2O$ as the standard for Ir (IV) state.

For *ex-situ* XPS measurements, the Na-$IrO_x(OH)_y$ thin film was also cycled in a PBS between -0.6 and 0.8 V with a slower rate (10 mV s^{-1}), followed by holding the potential at -0.15, 0.3, and 0.7 V for 1,000 s. The sample was rinsed with deionized water and dried using air blow immediately, and transferred into a vacuum chamber. A Kratos Axis Ultra DLD was used to conduct the initial survey scans and characterize the oxidation states of Ir, O, and Na near the surface of Na-$IrO_x(OH)_y$ thin film. For data processing, the XAS spectra were analyzed by Athena using its intensity normalization and curve merging/fitting functions, whereas the XPS profiles were fitted using CASA software.

Cytotoxicity tests during device operation

Cytotoxicity test was performed with L929 mouse lung fibroblasts on Na-$IrO_x(OH)_y$-Au-PPMM samples, and the cell

viability test involved the CellTiter 96® AQueous One Solution Cell Proliferation Assay Kit (Promega Co.) and 3-(4,5-dimethylthiazol-2-yl)-5-(3-carboxymethoxyphenyl)-2-(4-sulfophenyl)-2H-tetrazolium (MTS). Each sample was cleaned by UV-light exposure for 12 h, followed by dicing into 0.8×0.8 cm^2 electrodes, and the L929 cells were incubated for 24 h before tested. A 48-well plate was used for the experiment, each well was seeded with 400 µL cell suspension, and was cultured at 37°C in a humidified atmosphere of 5% CO_2 in air for 1, 4, and 7 days. The L929 cell suspension had a cell concentration of 104 cells mL^{-1}, and was composed of 99 vol% of Dulbecco's Modified Eagle Medium (DMEM; Sigma-Aldrich) and 1 vol% of antibiotic (Antibiotic-Antimycotic (100X), Gibco™). After treatment, the entire cell suspension was removed and the 48-well plate was rinsed three times with PBS. The 48-well plate was then filled with MTS solution (20 vol% MTS and 80 vol% DMEM), and was incubated for 1 h at 37°C to produce formazan crystals. The formazan crystals indicating the number of living cells exhibited a characteristic absorption peak, while the optical density readings were obtained using a multi-well scanning spectrophotometer (EpochTM 2, BioTek Instruments Inc.). The absorbance was monitored at 495 nm, and compared with the cells in control group to obtain the cell viability.

The performance of Na-$IrO_x(OH)_y$ full cell and its cytotoxicity were also examined with MTS tests in a 6-well plate. As shown in Figure 5a, a layer of hydrophilic PTFE membrane was sandwiched between two Na-$IrO_x(OH)_y$-Au-PPMM electrodes (1×2 cm^2) to prevent short circuit. The assembled open system full cell was soaked in 8 mL L929 solution with an effective area of 1×1 cm^2, and was subjected to continuous cycling test. Two parameters were imposed on the sample, the first was a 4 h test in which the full cell was continuously run with different GCD scanning rates, ranging from 0.05 to 1 mA cm^{-2}, and the other was a 3-day test, which the sample was kept to a continuous charge-discharge test at 0.1 mA cm^{-2}. After experiments, the cells followed the MTS test mentioned above to measure any cytotoxicity while the full cell was functioning.

Results and discussion

Materials and Characterization

The scanning electron microscope (SEM) image in Figure 1a displays the as-synthesized Na-$IrO_x(OH)_y$ thin film with a uniform thickness of 30 nm. To investigate the structural evolution of Na-$IrO_x(OH)_y$ as a function of annealing temperature, *in-situ* X-ray diffraction (XRD), thermogravimetric analysis (TGA), and Fourier-transform infrared spectroscopy (FT-IR) were carried out on the as-synthesized sample in ambient atmosphere. The *in-situ* XRD in Figure 1b shows that the as-synthesized Na-IrOx(OH)y is amorphous since only two broad diffraction signals at 33° and 59° (2θ) caused by the capillary holder were observed. The amorphous structure remained intact until 450°C after which, at higher temperatures, distinct peaks for crystalline rutile IrO_2 (ICSD-81028) emerged. The rutile phase remained stable up to 600°C. TGA analysis for Na-$IrO_x(OH)_y$ powders indicated a gradual weight loss until 600°C (Figure 1c). Since the sample was prepared from an aqueous bath, the weight loss before 100°C was attributed to the surface-adsorbed water, and only the weight removed above 100°C was due to the hydrated water in amorphous Na-$IrO_x(OH)_y$. Given the rutile IrO_2 found at 600°C (Figure 1b) and considering that the Na was still present in the sample, the weight of structural water was determined to be 7.17 wt%, which is close to $IrO_2 \cdot xH_2O$ with x = 1. In terms of elemental analysis, energy-dispersive X-ray spectroscopy (EDX) in Figure S1 revealed the composition of Na, Ir, and O, while the FT-IR spectrum in Figure 1d confirmed the various constituents of the as-synthesized Na-$IrO_x(OH)_y$ by revealing distinct signals for Ir-O bonding (565 cm^{-1}) and Ir-OH bonding (1,410 and 1,560 cm^{-1}). In comparison, the FT-IR spectrum in Figure S2 for rutile IrO_2 annealed at 600°C only showed the Ir-O peak (565 cm^{-1}).

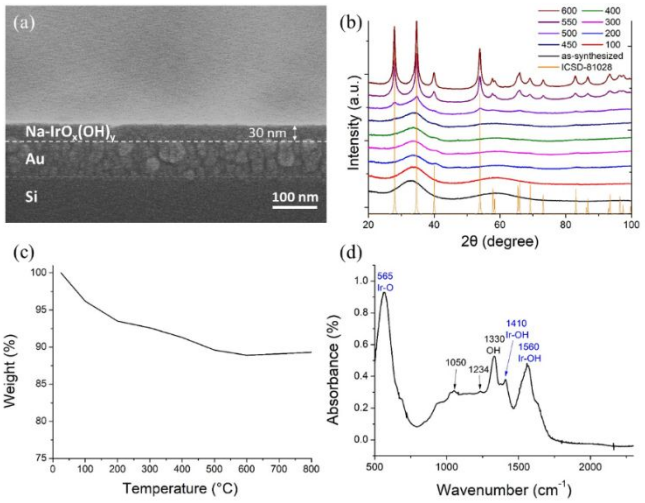

Figure 1. Material characterization of Na-$IrO_x(OH)_y$. (a) SEM cross-sectional image of as-synthesized Na-$IrO_x(OH)_y$ with a thickness of 30 nm. (b) *In-situ* XRD patterns of Na-$IrO_x(OH)_y$ sintered at different temperatures. An ICSD database of rutile IrO_2 is also shown as the reference. (c) TGA curve of Na-$IrO_x(OH)_y$ powders from 25 to 600°C in air with a ramp rate of 5°C/min. (d) FT-IR analysis of as-synthesized Na-$IrO_x(OH)_y$.

Electrochemical Characterization

Cyclic voltammetry (CV) profiles for Na-$IrO_x(OH)_y$ thin films in sweep rates between 1 and 50 mV s^{-1} are shown in Figure 2a. These experiments were carried out in a 3-electrode configuration in which the PBS, Pt mesh, and saturated Ag/AgCl were used as the electrolyte, counter electrode, and reference electrode, respectively (details in the Experimental Section). The Na-$IrO_x(OH)_y$ clearly exhibited two pairs of redox signals, different from that of a sputtered crystalline IrO_x (Figure S3a). Figure 2b summarizes the areal and gravimetric capacity for the Na-$IrO_x(OH)_y$ derived from the CV profiles in Figure 2a. The Na-$IrO_x(OH)_y$ demonstrated a capacity of nearly 1,200 C g^{-1} (~ 14 mC cm^{-2}) at 1 mV s^{-1}, which was over 40% greater than the theoretical capacity of IrO_2 (860 C g^{-1}), assuming a 2-electron transfer process.[23,34,42,43] To confirm the CV results, the gravimetric capacity of Na-IrOx(OH)y was also determined using a sample prepared under the same synthesis condition on an electrochemical quartz crystal microbalance (eQCM) substrate,

which was capable of measuring the actual sample weight. Figure S4 displays the weight change on the eQCM substrate, where the areal loading of Na-$IrO_x(OH)_y$ was 10.4 μg cm^{-2} after 1 h of deposition.

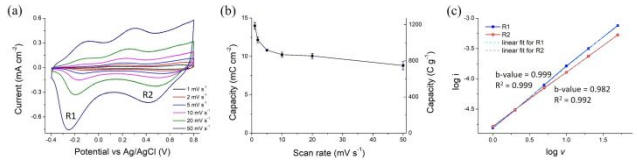

Figure 2. Electrochemical analysis of Na-$IrO_x(OH)_y$ on an Au-coated Si substrate. (a) CV profiles of Na-$IrO_x(OH)_y$ at different scan rates in PBS. (b) CV-derived capacity as a function of scan rate for Na-$IrO_x(OH)_y$. (c) The log *v*-log i correlation derived from the reduction peaks as marked as R1 and R2 in Figure 2a.

To understand the charge storage mechanism of Na-$IrO_x(OH)_y$, the peak currents from different scan rates (*v*) were analyzed using the following power law relationship[21]:

$$i = a\,v^b \qquad (6)$$

where the b value provides insight as to whether the charge storage mechanism is diffusion-controlled (b = 0.5) or surface-controlled (b = 1). The log *v*-log i plot in Figure 2c displayed a linear dependence of peak current on sweep rate indicating that the b values for those two reduction redox peaks (marked as R1 and R2 in Figure 2a) had values that were nearly 1. The analyzed results of the oxidation peaks were also listed in Figure S5. These values suggested that the redox reaction for Na-$IrO_x(OH)_y$ followed a surface-controlled process. The same study was also conducted on a sputtered IrO_x thin film (Figure S3b and Figure S3c) and smaller b values, 0.81 for reduction and 0.76 for oxidation, were recorded. Based on prior work, it is likely that the different behavior was caused by the absence of a hydrous boundary and a decrease in conductivity, making proton diffusion sluggish.[21,27,44]

Redox Reactions of Na-$IrO_x(OH)_y$

We carried out a series of experiments including *operando* X-ray absorption spectroscopy (XAS), *ex-situ* X-ray photoelectron spectroscopy (XPS), and eQCM to determine the cause of additional capacity of the Na-$IrO_x(OH)_y$ thin films. The *operando* XAS enabled us to determine the valence change of Ir during the redox reactions. The analysis was performed at potentials held at -0.15, 0.3, and 0.7 V (vs Ag/AgCl) based on the CV profile taken at 1.0 mV s^{-1} of Na-$IrO_x(OH)_y$ (Figure 3a). The X-ray absorption near edge structure (XANES) profile (Figure 3b, full spectra in Figure S6) indicated that the Ir valence state in Na-$IrO_x(OH)_y$ was changing during the CV scans as there were shifts in the Ir absorption energy. Specifically, the Na-$IrO_x(OH)_y$ at 0.3 V retained the Ir (IV) state by exhibiting a peak energy at 11,219.5 eV identical to the standard $IrO_2{\cdot}H_2O$ powder used as a reference. In addition, clear peak shifts at the end of the cathodic (-0.15 V) and anodic scans (0.7 V) were observed. The shift in the absorption peak energy indicated that valence changes of Ir (III/IV) and Ir (IV/V) were taking place at -0.15 and 0.7 V, respectively.

Ex-situ XPS carried out on the Na-$IrO_x(OH)_y$ thin film was used to determine the valence states of Na and O at different potentials. The results as shown in Figure 3c and Figure 3d along with the survey scan in Figure S7 and Table SI. The peak for Na 1s was detected at 0.3 and 0.7 V, but not at -0.15 V. The absence of Na at the lower potential suggested that the Na ions were participating in the redox reactions, and are thus contributing to the additional capacity in Na-$IrO_x(OH)_y$. Our approach to obtaining the oxygen stoichiometry is summarized in the Supplementary Information, while the XPS results for the O 1s are shown in Figure 3d and Figure S8, respectively.

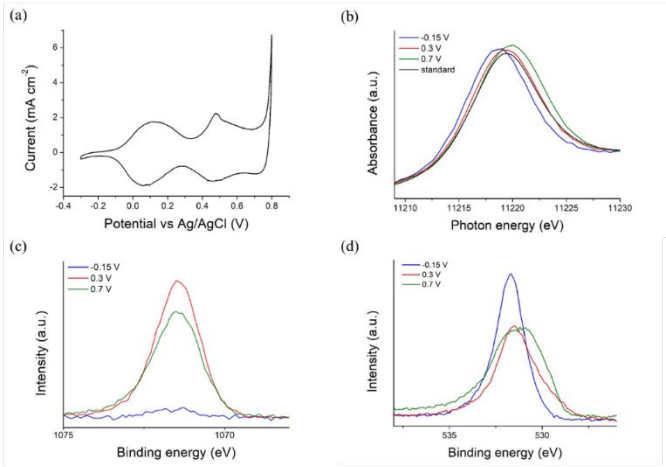

Figure 3. *Operando* XAS and *ex-situ* XPS analysis of Na-$IrO_x(OH)_y$. (a) CV profile of Na-$IrO_x(OH)_y$ on ITO at 1 mV s^{-1} in PBS recorded during XAS analysis. (b) Ir L_{III}-edge XANES of Na-$IrO_x(OH)_y$ with potential holding at -0.15, 0.3, and 0.7 V, respectively. The spectrum of commercial $IrO_2{\cdot}H_2O$ powder is listed as the standard for comparison. (c) *Ex-situ* XPS Na 1s spectra measured at different potentials. (d) *Ex-situ* XPS O 1s spectra measured at different potentials.

The eQCM measurements effectively establish the mass change associated with the charge storage process for Na-$IrO_x(OH)_y$. These experiments also used a three-electrode arrangement in which the Na-$IrO_x(OH)_y$-coated quartz crystal, Pt, and Ag/AgCl were used as the working electrode, counter electrode, and reference electrode. In contrast to the CV experiments that used PBS, the eQCM measurements were operated with a 0.5 M Na_2HPO_4 aqueous solution to highlight the sodium contribution without interference from the cations typically present in the PBS. A minimum scan rate of 10 mV s^{-1} was imposed due to the resolution limitation of the eQCM with regard to the signal-to-noise ratio for the charge and frequency changes. The increased frequency of the coated quartz electrode (Figure 4a) during Ir oxidation (Ir (III/V)), from -0.4 to 0.6 V (vs Ag/AgCl), indicated that the Na-$IrO_x(OH)_y$ exhibits a steady weight loss. Upon reduction over this same potential range, the frequency change followed an identical pattern back to zero. This negligible variation in weight suggests that the fast redox reactions on Na-$IrO_x(OH)_y$ were highly reversible without any undesirable side reaction. From Figure 4a, we derived the mass change as a function of charge (Figure 4b), where the slope reflects the actual reacting species. Prior research has

shown that as the IrO_2 undergoes a protonation step, the charge transfer responsible for a single valence change of Ir was correlated with a mass change of 1 g mol^{-1},[23] consistent with there being a single proton involved. During the oxidation scan, the mass change of Na-$IrO_x(OH)_y$ from -0.4 to 0.6 V exhibited two different slopes. The slope across the lower-voltage redox reaction showed a weight loss of 1.35 g mol^{-1}, whereas the slope over the higher-voltage reaction showed a weight loss of 1.06 g mol^{-1}. These weight changes were reversible and identical amount of weight gains were recorded during the reduction scan. These results indicate that an additional species, other than the protonation reaction, is involved with the redox reactions of Na-$IrO_x(OH)_y$. While the mass difference between these two slopes does not give the precise molecular weight of sodium, it is quite close. Thus, combining the eQCM results with *ex-situ* XPS, we consider there to be good evidence that sodium insertion into $Ir(OH)_3$ is responsible for the extra charge storage capacity.

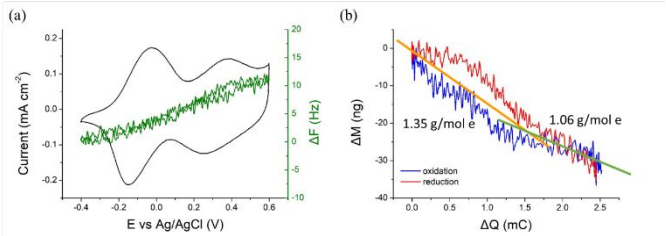

Figure 4. eQCM analysis for Na-$IrO_x(OH)_y$ in 0.5 M Na_2HPO_4 aqueous solution with a scan rate of 10 mV s^{-1}. (a) CV profile between -0.4 and 0.6 V, and corresponding frequency change recorded by eQCM. (b) Variation in mass as a function of coulomb charge change from CV profile.

Symmetric Full Cell of Na-$IrO_x(OH)_y$

The Na-$IrO_x(OH)_y$ full cell was based on the conformal coating of Na-$IrO_x(OH)_y$ on a flexible Au-coated polypropylene micromembrane (Au-PPMM) which served as a biocompatible current collector (Figure S9). The deposition process on the Au-PPMM was repeated 5 times with each deposition using a fresh plating solution to achieve a Na-$IrO_x(OH)_y$ total loading of ~1 mg cm^{-2}. To fabricate a full cell, two Na-$IrO_x(OH)_y$-Au-PPMM electrodes were separated by a hydrophilic polytetrafluoroethylen (PTFE) membrane (Figure 5a). The full cells were evaluated either in a PBS or in an *in-vivo* aqueous solution containing L929 mouse lung fibroblast cells (L929 solution), and their resulting impedance spectra are displayed in Figure 5b. The Nyquist plots were fitted using an equivalent circuit model in Figure S10, which contained an electrolyte resistance (Rs), a charge-transfer resistance (Rct), a constant phase element (CPE), and a Warburg element (Ws) for ionic diffusion. Table SII shows that the various circuit parameters are within 15 to 20% of each other. Figure 5c displays the galvanostatic charge-discharge (GCD) profiles for the full cell. The cell was capable of storing an areal capacity of 282 mC cm^{-2} (78 μAh cm^{-2}) at a current density of 50 μA cm^{-2} and approximately 35% of this areal capacity is retained at 1 mA cm^{-2} (84 mC cm^{-2}; 23 μAh cm^{-2}). Extended deep-cycle tests for 50 cycles were carried out at 100 μA cm^{-2}, where the full cell retained 225 mC cm^{-2} in both L929 solution (Figure 5d) and PBS (Figure S11). We have further tested the full cell using CV at 50 mV s^{-1} in PBS for high power applications, as shown in Figure S12, where the cell stored 76 mC cm^{-2} in 32 sec and retained over 97% of the capacity after 10,000 cycles. These results demonstrate the excellent stability of Na-$IrO_x(OH)_y$ full cells under an open system environment.

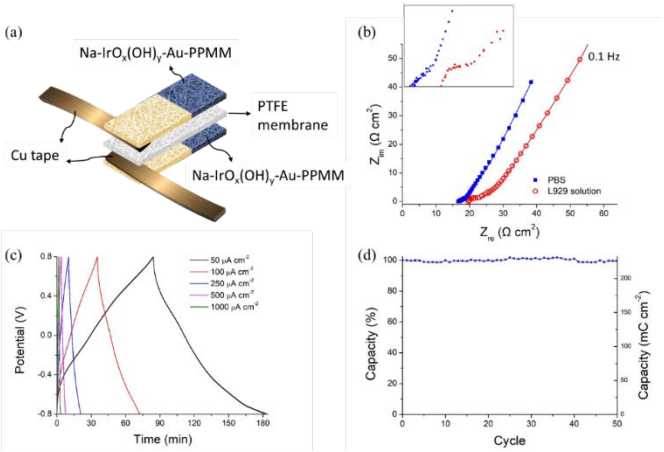

Figure 5. Electrochemical performance of Na-$IrO_x(OH)_y$ full cell. (a) A schematic of Na-$IrO_x(OH)_y$-Au-PPMM/PTFE/Na-$IrO_x(OH)_y$-Au-PPMM open system full cell. (b) Nyquist plot of Na-$IrO_x(OH)_y$ full cell in PBS and in L929 solution. Inset shows a magnified plot at high frequency. (c) GCD performances in L929 solution. (d) Capacity retention during the long term cycling test at 100 μA cm^{-2} in L929 solution.

Cytotoxicity tests were based on subjecting the Na-$IrO_x(OH)_y$-Au-PPMM electrode to a standard MTS test using the L929 mouse lung fibroblasts, the experiment setup is shown in Figure 6a.[45] During the test, the cells were cultured on top of the electrode for 1, 3, and 7 days, and the cell viability was assessed by measuring the optical density of resulting solution at 495 nm. Figure 6b displays the cell viability percentage calculated by optical density ($OD_{sample}/OD_{control}$), showing the cell viability was 94.4%, 98.1%, and 99.9% after 1, 4, and 7 days, respectively. We further tested the cytotoxicity of the full cell under two operational conditions, i.e., the L929 cells were cultured during the cytotoxicity test near the Na-$IrO_x(OH)_y$-Au-PPMM electrodes which were being cycled concurrently using two different GCD protocols. Figure 6c displays the GCD protocols conducted in L929 solution, including a 4-hour current pulse test and a 3-day long-term operation test, and the corresponding cell viability results are summarized in Figure 6d. For the 4-hr test, the L929 cells survived on Na-$IrO_x(OH)_y$ under charge/discharge current, including 50, 100, 200, 500, and 1,000 μA cm^{-2}. The 4-hr test result indicated a negligible toxic effect on the L929 cells by showing a cell viability of 98.3% (Figure 6d, left). For the long-term operational test, the L929 cells sustained a full cell that was charged and discharged between 0% and 80% capacity for 50 cycles at 100 μA cm^{-2}. After three days (Figure 6d, right), the cells were able to proliferate and reached a viability of 101.1%, indicating that the package-

free full cell was functioning reliably under the open system environment without any biocompatibility concern.

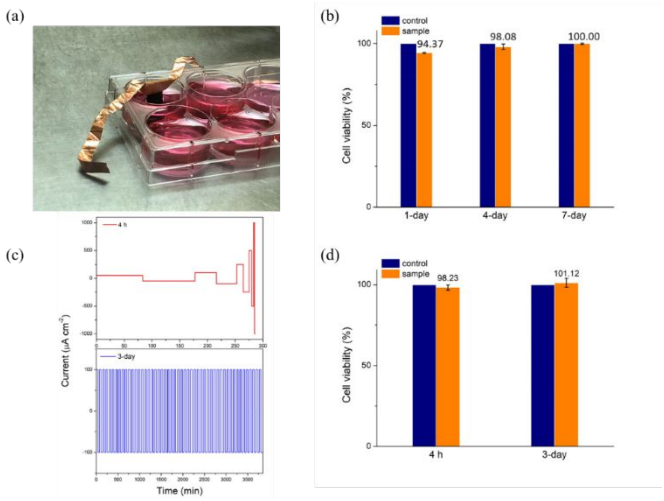

Figure 6. Cytotoxicity test for Na-IrO$_x$(OH)$_y$ full cell. (a) Experiment setup for continuous electrochemical testing on a Na-IrO$_x$(OH)$_y$ device during cell culture. (b) Standard cytotoxicity test of Na-IrO$_x$(OH)$_y$ thick film deposited on Au coated PMS for 1, 4, and 7 days. (c) i-t performances during GCD in L929 solution. (d) MTS test results during Na-IrO$_x$(OH)$_y$ full cell operation with continuous GCD for 4 h and 3 days.

Comparison of Implantable Power Sources

The Na-IrO$_x$(OH)$_y$-Au-PPMM open system full cell has demonstrated greater energy and power density over any of the reported open system supercapacitors listed in Table SIII. Moreover, with the extended cycle life and package-free design, the usable energy could potentially surpass that of state-of-the-art implantable batteries. A Ragone plot in Figure 7a further summarizes the performance of Na-IrO$_x$(OH)$_y$ full cell with similar implantable energy storage devices in volumetric energy density and power density. With the device density of 0.5 g cm^{-3} built with two Au-PPMM electrodes (400 μm thick in total), the Na-IrOx(OH)y full cell has achieved either high energy density of 3.4 mWh cm^{-3} (at 2 mW cm^{-3}), a value that is comparable to most Li-ion thin film batteries[11,46] and 10 times greater than that of commercial EDLCs,[5-18,47,48] or high power density of 40 mW cm^{-3} (at 0.95 mWh cm^{-3}), a value that is forty times greater than that of Li-ion thin film batteries.[11] Because of the high energy density and power density, our sample is capable of powering implantable biomedical devices such as pacemakers (10–30 μW) and spinal cord stimulators (1 mW).[6]

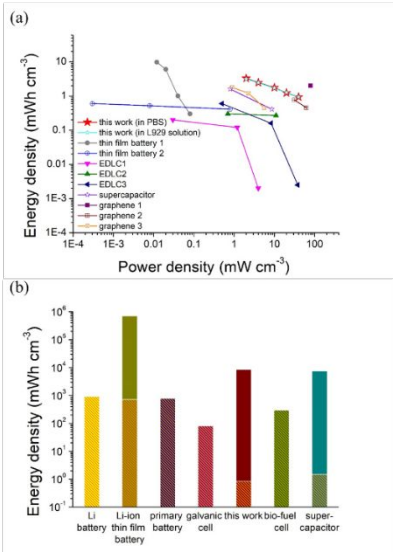

Figure 7. Performance comparisons of Na-IrO$_x$(OH)$_y$ full cell with other implantable energy storage devices. (a) Ragone plot of Na-IrO$_x$(OH)$_y$ and other implantable energy storage devices.[5-18,48,49] (b) Primary (grid line) and rechargeable (solid color) energy density for different implantable energy storage devices.[11,40,49-52]

Another important feature of Na-IrO$_x$(OH)$_y$ as an open system electrode is the extended cycle life. Figure 7b further compares the total usable energy among different implantable energy storage devices, including conventional close system batteries and existing open system batteries, supercapacitors, and fuel cells. As detailed in Table SIV, the usable energy for those reported devices was derived by multiplying its energy density by lifetime, literally the number of cycles where each device lost 20% of its initial energy. Different from the biogalvanic cells and biofuel cells, which are normally used for short term purpose such as drug delivery owing to their limited cycle life, our full cell which functions for 10,000 cycles (Figure S12) has demonstrated an accumulated energy of 8,480 mWh cm^{-3}. The large total usable energy of our Na-IrO$_x$(OH)$_y$ device suggests a considerable advantage over similar open-system counterparts by limiting device replacement surgeries.

Conclusions

In summary, Na-IrO$_x$(OH)$_y$, prepared using a wet chemical bath, was carefully investigated for its charge storage performance. In contrast to conventional IrO_2, the Na-IrO$_x$(OH)$_y$ stored a capacity of 1,187 C g^{-1} due to its hydrous nature and the Na dopants. A kinetic study showed that charge storage was governed by surface-controlled processes which enable high power to be achieved. The XPS and eQCM further revealed the participation of hydroxyl and sodium moieties in determining electrochemical properties and enabling an open structure favorable for proton migration. Furthermore, Na-IrO$_x$(OH)$_y$ was evaluated by both half-cell and full-cell testing on Au-coated wafers and Au-PPMMs, and an open system energy storage device was fabricated. A capacity of 295 mC cm^{-2} was achieved

in PBS, along with an energy density of 3.15 mWh cm^{-3}. These values were comparable with those of commercial Li-ion thin film batteries, while exceeding their power density. No evidence of cell toxicity was found after long-term observation, and the capacity remained stable after 10,000 cycles. These results show the promise of using the Na-$IrO_x(OH)_y$ open system full cell as an energy storage system for implantable electronics.

Author Contributions

Formal analysis, Y.H., K.T., S.C, G.J.W., C.S.C., W.C., C.C., and P.C.; Writing – Original Draft, Y.H. and C.M.L; Writing – Review & Editing, P.W. and B.S.D.; Supervision, J.L., S.C., B.S.D.,and P.W.

Conflicts of interest

There are no conflicts to declare.

Acknowledgements

Authors would like to acknowledge the support of this research from the Ministry of Science and Technology (MOST) in Taiwan (Dragon Gate Program: 108-2911-I-009-516), the Office of Naval Research (N00014-19-1-2113) in USA, as well as the Higher Education Sprout Project by the Ministry of Education (MOE) in Taiwan for "Center for Neuromodulation Medical Electronics Systems" and the Higher Education Sprout Project of the National Yang Ming Chiao Tung University and MOE, Taiwan. The authors would also like to thank Mr. Chung-Kai Chang in NSRRC for SXRD analysis.

References

1 H. Habibzadeh, K. Dinesh, O. R. Shishvan, A. Boggio-Dandry, G. Sharma, and T. Soyata, *IEEE Internet Things J.*, 2020, **7**, 53-71.
2 M. Haghi, K. Thurow, and R. Stoll, *Healthc. Inform. Res.*, 2017, **23**, 4-15.
3 M. N. Bhuiyan, M. M. Rahman, M. M. Billah, and D. Saha, *IEEE Internet Things J.*, 2021, **8**, 10474-10498.
4 A. Walcarius, S. D. Minteer, J. Wang, Y. Lin, and A. Merkoci, *J. Mater. Chem. B*, 2013, **1**, 4878-4908.
5 D. C. Bock, A. C. Marschilok, K. J. Takeuchi, and E. S. Takeuchi, *Electrochim. Acta*, 2012, **84**, 155-164.
6 S. Y. Yang, V. Sencadas, S. S. You, N. Z. X. Jia, S. S. Srinivasan, H. W. Huang, A. E. Ahmed, J. Y. Liang, and G. Traverso, *Adv. Funct. Mater.*, 2021, **31**, 2009289.
7 W. Greatbatch, J. H. Lee, W. Mathias, M. Eldridge, J. R. Moser, and A. A. Schneider, *IEEE. Trans. Biomed. Eng.*, 1971, **5**, 317-324.
8 A. B. Amar, A. B. Kouki, and H. Cao, *Sensors*, 2015, **15**, 28889-28914.
9 H. Sheng, X. Zhang, J. Liang, M. Shao, E. Xie, C. Yu, and W. Lan, *Adv. Healthc. Mater.*, 2021, **10**, 2100199.
10 X. Huang, L. Wang, H. Wang, B. Zhang, X. Wang, R. Y. Z. Stening, X. Sheng, and L. Yin, *Small*, 2020, **16**, 1902827.
11 I. M. Mosa, A. Pattammattel, K. Kadimisetty, P. Pande, M. F. El-Kady, G. W. Bishop, M. Novak, R. B. Kaner, A. K. Basu, C. V. Kumar, and J. F. Rusling, *Adv. Energy Mater.*, 2017, **7**, 1700358.
12 H. Sheng, J. Zhou, B. Li, Y. He, X. Zhang, J. Liang, J. Zhou, Q. Su, E. Xie, W. Lan, K. Wang, and C. Yu, *Sci. Adv.*, 2021, **7**, eabe3097.
13 H. J. Sim, C. Choi, D. Y. Lee, H. Kim, J.-H. Yun, J. M. Kim, T. M. Kang, R. Ovalle, R. H. Baughman, C. W. Kee, and S. J. Kim, *Nano Energy*, 2018, **47**, 385-392.
14 S. He, Y. Hu, J. Wan, Q. Gao, Y. Wang, S. Xie, L. Qiu, C. Wang, G. Zheng, B. Wang, and H. Peng, *Carbon*, 2017, **122**, 162-167.
15 P. Kumar, E. Di Mauro, S. Zhang, A. Pezzella, F. Soavi, C. Santato, and F. Cicoira, *J. Mater. Chem. C*, 2016, **4**, 9516-9525.
16 J. S. Chae, N.-S. Heo, C. H. Kwak, W.-S. Cho, G. H. Seol, W.-S. Yoon, H.-K. Kim, D. J. Fray, A. T. E. Vilian, Y.-K. Han, Y. S. Huh, and K. C. Roh, *Nano Energy*, 2017, **34**, 86-92.
17 F. Jin, T. Li, T. Yuan, L. Du, C. Lai, Q. Wu, Y. Zhao, F. Sun, L. Gu, T. Wang, and Z. Q. Feng, *Adv. Mater.*, 2021, **33**, 2104175.
18 M. Chen, X. Fu, Z. Chen, J. liu, W. and H. Zhong, *Adv. Funct. Mater.*, 2021, **31**, 2006744.
19 A. Zebda, J. P. Alcaraz, P. Vadgama, S. Shleev, S. D. Minteer, F. Boucher, P. Cinquin, and D. K. Martin, *Bioelectrochemistry*, 2018, **124**, 57-72.
20 D. Jiang, B. Shi, H. Ouyang, Y. Fan, Z. L. Wang, and Z. Li, *ACS Nano*, 2020, **14**, 6436-6448.
21 C. Choi, D. S. Ashby, D. M. Butts, R. H. DeBlock, Q. Wei, J. Lau, and B. Dunn, *Nat. Rev. Mater.*, 2020, **5**, 5-19.
22 Y. Zhou, H. Qi, J. Yang, Z. Bo, F. Huang, M. S. Islam, X. Lu, L. Dai, R. Amal, C. H. Wang, and Z. Han, *Energy Environ. Sci.*, 2021, **14**, 1854-1896.
23 A. J. Perez, R. Beer, Z. Lin, E. Salager, P.-L. Taberna, A. M. Abakumov, P. Simon, and J.-M. Tarascon, *Adv. Energy Mater.*, 2018, **8**, 1702855.
24 M. Dandekar, G. Arabale, and K. Vijayamohanan, *J. Power Sources*, 2005, **141**, 198-203.
25 S. M. Wellman, J. R. Eles, K. A. Ludwig, J. P. Seymour, N. J. Michelson, W. E. McFadden, A. L. Vazquez, and T. D. Y. Kozai, *Adv. Funct. Mater.*, 2018, **28**, 1701269.
26 S. F. Cogan, *Annu. Rev. Biomed. Eng.*, 2008, **10**, 275-309.
27 H. Jang and J. Lee, *J. Energy Chem.*, 2020, **46**, 152-172.
28 E. Slavcheva, R. Vitushinsky, W. Mokwa, and U. Schnakenberg, *J. Electrochem. Soc.*, 2004, **151**, E226.
29 D. Liu, S. Yu, S. Son, and S. Joo, *ECS Trans.*, 2008, **16**, 103.
30 A. Ghazavi, J. Maeng, M. Black, S. Salvi, and S. F. Cogan, *J. Neural. Eng.*, 2020, **17**, 016022.
31 S. F. Cogan, J. Ehrlich, T. D. Plante, A. Smirnov, D. B. Shire, M. Gingerich, and J. F. Rizzo, *J. Biomed. Mater. Res. Part B Appl. Biomater.*, 2009, **89**, 353-361.
32 S. F. Cogan, P. R. Troyk, J. Ehrlich, and T. D. Plante, *IEEE Trans. Biomed. Eng.*, 2005, **52**, 1612-1614.
33 S. F. Cogan, A. A. Guzelian, W. F. Agnew, T. G. Yuen, and D. B. McCreery, *J. Neurosci. Methods*, 2004, **137**, 141-150.
34 L. D. Burke and D. P. Whelan, *J. Electroanal. Chem. Interf. Electrochem.*, 1984, **162**, 121-141.
35 S. A. Beknalkar, A. M. Teli, N. S. Harale, D. S. Patil, S. A. Pawar, J. C. Shin, and P. S. Patil, *Appl. Surf. Sci.*, 2021, **546**, 149102.
36 W. Sun, Y. Song, X.-Q. Gong, L.-M. Cao, and J. Yang, *ACS Appl. Mater. Interfaces.*, 2016, **8**, 820-826.
37 Q. Qin, H. Jang, Y. Wang, L. Zhang, Z. Li, M. G. Kim, S. Liu, X. Liu, and J. Cho, *Adv. Energy Mater.*, 2021, **11**, 2003561.
38 C. A. Amarnath, N. Venkatesan, M. Doble, and S. N. Sawant, *J. Mater. Chem. B*, 2014, **2**, 5012-5019.
39 H. Li, C. Zhao, X. Wang, J. Meng, Y. Zou, S. Noreen, L. Zhao, Z. Liu, H. Ouyang, P. Tan, M. Yu, Y. Fan, Z. L. Wang, and Z. Li, *Adv. Sci.*, 2019, **6**, 1801625.
40 P. Nadeau, D. El-Damak, D. Glettig, Y. L. Kong, S. Mo, C. Cleveland, L. Booth, N. Roxhed, R. Langer, A. P. Chandrakasan, and G. Traverso, *Nat. Biomed. Eng.*, 2017, **1**, 1-8.
41 C. H. Kwon, Y. Ko, D. Shin, M. Kwon, J. Park, W. K. Bae, S. W. Lee, and J. Cho, *Nat. Commun.*, 2018, **9**, 4479.

42 A. R. Hillman, M. A. Skopek, and S. J. Gurman, *Phys. Chem. Chem. Phys.*, 2011, **13**, 5252-5263.
43 C. E. Moore, F. Afsahi, A. P. Young, and E. L. Gyenge, *J. Phys. Chem. C*, 2019, **123**, 23361-23373.
44 S. S. Thanawala, R. J. Baird, D. G. Georgiev, and G. W. Auner, *Appl. Surf. Sci.*, 2008, **254**, 5164-5169.
45 G. Malich, B. Markovic, and C. Winder, *Toxicology*, 1997, **124**, 179-192.
46 G. Qian, B. Zhu, X. Liao, H. Zhai, A. Srinivasan, N. J. Fritz, Q. Cheng, M. Ning, B. Qie, Y. Li, S. Yuan, J. Zhu, X. Chen, and Y. Yang, *Adv. Mater.*, 2018, **30**, 1704947.
47 N. R. Chodankar, D. P. Dubal, G. S. Gund, and C. D. Lokhande, *J. Energy Chem.*, 2016, **25**, 463-471.
48 Q. Zhou, X. Ye, Z. Wan, and C. Jia, *J. Power Sources*, 2015, **296**, 186-196.
49 T. Reddy, *Linden's Handbook of Batteries*, in chapter 14: Lithium primary batteries, McGraw Hill Professional, New York, 2010, 14.1–14.90.
50 M. S. Whittingham, *Proc. IEEE*, 2012, **100**, 1518-1534.
51 R. J. Brodd, K. R. Bullock, R. A. Leising, R. L. Middaugh, J. R. Miller, and E. Takeuchi, *J. Electrochem. Soc.*, 2004, **151**, K1.
52 S. El Ichi-Ribault, J.-P. Alcaraz, F. Boucher, B. Boutaud, R. Dalmolin, J. Boutonnat, P. Cinquin, A. Zebda, and D. K. Martin, *Electrochim. Acta*, 2018, **269**, 360-366.